Large-Eddy Simulation of Turbulent Flow over an Axisymmetric Hill

Nayan Patel*and Suresh Menon†
School of Aerospace Engineering
Georgia Institute of Technology
Atlanta, Georgia, USA 30332

Large-Eddy Simulation (LES) of high Reynolds number turbulent flow over an axisymmetric hill of height $H = 2\delta$, where δ is the incoming turbulent boundary layer thickness, is presented in this paper. Surface mean pressure, flow visualization and mean velocity profiles are presented and compared with experiments. In general, good agreement is obtained for the surface mean pressure and axial flow profiles. Analysis of the results show that multiple separation and reattachments occur on the lee-side of the hill. These results are also consistent with experimental observations, although there are some differences. The flow field is further analyzed to understand the dynamics of the flow.

1 Introduction

Three-dimensional (3D) unsteady separation and re-attachment of a high Reynolds (Re) number turbulent boundary is studied here using Large-Eddy Simulation (LES). In particular, turbulent flow over an axisymmetric hill of height $H = 2\delta$, is investigated here. High Reynolds number flows past such obstacles are of considerable interest due to their relevance for naval applications. Experimental studies of similar configurations by Simpson *et al.*[1] suggested that complex 3D vortical flow, and multiple separation and re-attachment occurs over a large area on the lee-side of the hills. They[2] also note that geometrically similar hills (H=2δ and H=δ) yield qualitatively and quantitatively dissimilar flow dynamics. This hints at the level of complexity associated with flows past such simple shapes.

Due to the highly unsteady nature of this flow, steady state Reynold-Averaged Navier Stokes (RANS) cannot be employed to study this flow. On the other hand, Direct Numerical Simulation (DNS) is computationally prohibitive. Here, we explore the ability of a LES method to capture the flow dynamics. Since the interest here is on high Re boundary layer, the near wall region must be properly resolved in order capture the physics. Past LES of high Re turbulent boundary

*Graduate Student, School of Aerospace Engineering; Student Member, AIAA
†Professor, School of Aerospace Engineering; Associate Fellow, AIAA

layers have not proven successful in capturing the near wall physics without resorting to very high resolution.[3,4,5] Many near-wall models have been proposed[6,7,8] for LES application but so far such models have not proven very successful. More recently,[9,10] a new two-level simulation (TLS) has been proposed to address the near-wall region within a LES context. However, none of these approaches have been used so far to study the current flow of interest.

In earlier studies,[11,12,13] a localized dynamic subgrid model based on the one-equation transport model for the subgrid kinetic energy was developed and applied to many high Re flows. This model (denoted hereafter LDKM) has also been applied to many reacting flow problems[14,15,16,17] and has demonstrated stability and accuracy in both near-wall and free shear regions. Here, we investigate the ability of the LDKM closure for resolving this high-Re flow.

First, we present the numerical model which includes description of the LES scheme used as well as the details of the computational domain used in the simulation. We then present the results of the simulation and discuss some of the interesting features observed. And finally, the paper ends with conclusions and some discussion of the scope of future studies in this area.

2 Simulation Model

In LES, all scales of motion larger than the grid resolution are resolved in space and time by the numerical scheme and the effect of the unresolved scales on the resolved motion are modelled in the LES equations. The choice of the governing equations to employ depends upon the problem of interest. In the present case, we are investigating low-speed, non-reacting flow. Hence, the incompressible Navier-Stokes equations would be the appropriate governing equations. However, in the present study, we employ the full compressible Navier-Stokes equations for two reasons: (a) we have an efficient parallel compressible LES solver (fourth-order accurate in space and second-order accurate in time) that has been extensively validated in both non-reacting[18] and reacting flows.[14,15,17] (Note that, the flow speed in a typical gas turbine is very low, 20-30 m/s.), and (b) we are also interested in determining if there is any acoustic signature associated with the 3D vortical flow separation and re-attachment.

A compressible solver allows for proper coupling between acoustics and fluid flow, and earlier studies[19] suggest that free vortices generate a quadrupole acoustic radiation but vortex interaction with a wall can generate dipole radiation (which is stronger). The present paper focusses primarily on the ability of the LDKM approach (not the numerical scheme) to predict accurately the flow physics. Comparison with experimental data is carried out to demonstrate the ability of the model. The analysis of the near-field acoustics will be reported in the near future.

The unsteady, compressible, exact Navier-Stokes equations governing the fluid flow (Eulerian approach) are presented below. Employing tensor notation, the conservation equation for mass, momentum, and energy are, respectively:

$$
\begin{aligned}
\frac{\partial \rho}{\partial t} &= -\frac{\partial \rho u_i}{\partial x_i} \\
\frac{\partial \rho u_i}{\partial t} &= -\frac{\partial}{\partial x_j}[\rho u_i u_j + p\delta_{ij} - \tau_{ij}] \\
\frac{\partial \rho E}{\partial t} &= -\frac{\partial}{\partial x_i}[(\rho E + p)u_i + q_i - u_j \tau_{ji}]
\end{aligned} \tag{1}
$$

where ρ is the mass density, p is the pressure, E is the total energy per unit mass, u_i is the velocity vector, q_i is the heat flux vector, and τ_{ij} is the viscous stress tensor. These equations are completed with the following relations:

$$\tau_{ij} = \mu(\frac{\partial u_i}{\partial x_j} + \frac{\partial u_j}{\partial x_i}) - \frac{2}{3}\mu(\frac{\partial u_k}{\partial x_k})\delta_{ij} \tag{2}$$

$$q_i = -\kappa \frac{\partial T}{\partial x_i} \tag{3}$$

$$P = \rho R T \tag{4}$$

$$E = C_v T + \frac{1}{2}u_k^2 \tag{5}$$

$$\mu = \mu_o(\frac{T}{T_o})^{3/2} \ \frac{T_0 + 110}{T + 110} \tag{6}$$

$$\kappa = \frac{\mu C_p}{Pr} \tag{7}$$

Here, μ, κ, C_p, and Pr are, respectively, the molecular viscosity (approximated by Sutherland's Law), the thermal conductivity, the specific heat at pressure and the Prandtl number ($Pr = 0.72$ for air).

These equations can be treated as an exact mathematical model for the motion of perfect gases regardless of whether or not the flow is laminar or highly turbulent. However, DNS resolution is required to exactly recover the equations in a computational model. As this is not practical, a LES representation of the governing equations is therefore needed.

As briefly mentioned earlier, LES fully resolves the large-scale dynamics and employs models at the sub-grid level. Therefore, an operation is required which can separate or *filter* the governing Navier-Stokes equations into large-scale and *SGS* components. This is achieved, following Erlebacher *et al.*,[20] by applying a spatial filtering operation to the governing equations such that $f = \widetilde{f} + f''$. There, $\sim$ and $''$ denote the resolved super-grid and unresolved sub-grid quantities, respectively. The resolved super-grid quantities are determined by Favre filtering:

$$\widetilde{f} = \frac{\overline{\rho f}}{\overline{\rho}} \tag{8}$$

where the over-bar represents spatial filtering defined as

$$\overline{f(x_i,t)} = \int f(x_i',t) G_f(x_i,x_i') dx_i'. \tag{9}$$

Here, G_f is the filter kernel and the integral is over the entire computational domain. Applying this filtering operation (basically, a low-pass filter of local grid size $\overline{\Delta}$) to the Navier-Stokes equations, the following LES equations are obtained:

$$\begin{aligned}
\frac{\partial \overline{\rho}}{\partial t} &= -\frac{\partial \overline{\rho}\widetilde{u}_i}{\partial x_i} \\
\frac{\partial \overline{\rho}\,\widetilde{u}_i}{\partial t} &= -\frac{\partial}{\partial x_j}[\overline{\rho}\widetilde{u}_i\widetilde{u}_j + \overline{p}\,\delta_{ij} - \overline{\tau}_{ij} + \tau_{ij}^{sgs}] \\
\frac{\partial \overline{\rho}\widetilde{E}}{\partial t} &= -\frac{\partial}{\partial x_i}[(\overline{\rho}\widetilde{E} + \overline{p})\widetilde{u}_i + \overline{q}_i - \widetilde{u}_j\overline{\tau}_{ji} + H_i^{sgs} + \sigma_{ij}^{sgs}]
\end{aligned} \tag{10}$$

The sub-grid terms resulting from the filtering operation, denoted with super-script ^{sgs}, represent the small-scale effects upon the resolved-scales in the form of additional stresses and fluxes. The filtered velocity, $\widetilde{u}_i$, and temperature, $\widetilde{T}$, are used to approximate $\overline{\tau}_{ij}$ and $\overline{q}_i$, respectively. The resulting SGS terms, the sub-grid stress tensor, sub-grid heat flux, and unresolved viscous work are defined, respectively, as:

$$\begin{aligned}
\tau_{ij}^{sgs} &= \overline{\rho}[\widetilde{u_i u_j} - \widetilde{u}_i\widetilde{u}_j] \\
H_i^{sgs} &= \overline{\rho}[\widetilde{Eu_i} - \widetilde{E}\widetilde{u}_i] + [\overline{pu_i} - \overline{p}\widetilde{u}_i] \\
\sigma_i^{sgs} &= [\overline{u_j\tau_{ij}} - \widetilde{u}_j\overline{\tau}_{ij}].
\end{aligned} \tag{11}$$

2.1 Subgrid Closure

The subgrid terms, Eq. 11, require explicit modelling since the small-scale correlations are not known. Since, dissipation of the turbulent kinetic energy occurs primarily in the small-scales, an eddy viscosity ν_t model is employed. The simplest model is: $\nu_t = C_\nu l^{sgs} v^{sgs}$, where l^{sgs} and v^{sgs} are respectively, the characteristic length and velocity scale at the small-scale, and C_ν is a coefficient of proportionality. For LES, characteristic length scale is modelled as the local grid size, $\overline{\Delta}$ (= $(\Delta x_1 \Delta x_2 \Delta x_3)^{1/3}$).

Two approaches are popular for the specification of the velocity scale v^{sgs}: (a) the classical Smagorinsky's[21] algebraic model in which $v^{sgs} = \overline{\Delta}|\widetilde{S}_{ij}\widetilde{S}_{ij}|$, where $\widetilde{S}_{ij}$ is the resolved rate-of-strain

tensor, and (b) the subgrid kinetic energy approach of Schumann[22] in which $v^{sgs} = \sqrt{K^{sgs}}$, where K^{sgs} is the subgrid kinetic energy which is obtained by solving a transport equation along with the LES equations.

Past studies have demonstrated that since the algebraic model requires equilibrium between production and dissipation of energy (which occurs only in the dissipation region of the spectra), the grid resolution requirement can be quite severe, especially for the near-wall problem. Here, we employ the K^{sgs} based subgrid closure which has a significant advantage over the algebraic model since equilibrium between production and dissipation is not needed, and as a result, the grid scale cutoff can be in the inertial range.

This ability allows the use of the K^{sgs} subgrid closure to simulate high-Re flows using relative coarse grids, shown in many past studies.[13,15,18] The question that we wish to address in this study is how coarse one can go in the near-wall region of very high-Re flow when using the K^{sgs} model before the accuracy is compromised.

A transport equation for the subgrid kinetic energy (K^{sgs}), defined as $K^{sgs} = \frac{1}{2}[\widetilde{u_k^2} - \widetilde{u}_k^2]$ is:[11,13,23]

$$\frac{\partial \overline{\rho}\, K^{sgs}}{\partial t} + \frac{\partial}{\partial x_i}\left(\overline{\rho}\, \widetilde{u}_i K^{sgs}\right) = P^{sgs} - D^{sgs} + \frac{\partial}{\partial x_i}\left(\overline{\rho}\, \frac{\nu_t}{Pr_t}\frac{\partial K^{sgs}}{\partial x_i}\right) \tag{12}$$

were Pr_t is the turbulent Prandtl number which is assumed constant and equal to unity. Here, P^{sgs} and D^{sgs} are, respectively, the production and dissipation of K^{sgs}. The production term is defined as, $P^{sgs} = -\tau_{ij}^{sgs}(\partial \widetilde{u}_i/\partial x_j)$, where τ_{ij}^{sgs} is the modelled subgrid stress tensor,

$$\tau_{ij}^{sgs} = -2\overline{\rho}\,\nu_t(\widetilde{S}_{ij} - \frac{1}{3}\widetilde{S}_{kk}\delta_{ij}) + \frac{2}{3}\overline{\rho}K^{sgs}\delta_{ij}, \tag{13}$$

In the above expression, $\nu_t = C_\nu (K^{sgs})^{1/2}\overline{\Delta}$ and $\widetilde{S}_{ij}, = \frac{1}{2}(\partial \widetilde{u}_i/\partial x_j + \partial \widetilde{u}_j/\partial x_i)$ is the resolved rate-of-strain tensor. The dissipation term is modelled as $D^{sgs} = C_\varepsilon \overline{\rho}(K^{sgs})^{3/2}/\overline{\Delta}$.

There are two coefficients in this model, C_ν and C_ε that have to be either specified or determined dynamically as part of the solution. In the present study, we employ the aforementioned LDKM model to obtain these coefficients locally as a function of space and time. Although the LDKM model has been discussed in detail elsewhere,[11,13,14] for completeness, we summarize the key features of this model.

2.2 Localized Dynamic K-Equation Model (LDKM)

Experimental measurements in high Re turbulent jet[24] suggest that the subgrid stress τ_{ij}^{sgs} at the grid filter level $\overline{\Delta}$ and the Leonard's stress L_{ij} at the test filter level $\widehat{\Delta}(= 2\overline{\Delta})$ are self-similar. In the LDKM model, this observation is extended and it is assumed that L_{ij} and the subgrid stress $\widehat{\tau}_{ij^{sgs}}$ at the test filter level are also similar. Using this, $\widehat{\tau}_{ij^{sgs}}$ is modeled using the same form as for

τ_{ij}^{sgs} (Eq. 13), except that all variables are defined at the test filter level. Thus, for example, the subgrid kinetic energy at the test filter level is $k_{test} = \frac{1}{2}[\widehat{\widetilde{u_k^2}} - \widehat{\widetilde{u}_k}^2]$ and this quantity is fully resolved at the test filter $\widehat{\Delta}$ level. Thus, a direct (but over determined) expression for the model coefficient C_ν is obtained:

$$C_\nu = \frac{L'_{ij} M_{ij}}{2 M_{ij} M_{ij}} \tag{14}$$

Here, a least-square method is employed to obtain C_ν. In the above expression

$$L'_{ij} = L_{ij} - \frac{2}{3}\widehat{\overline{\rho}}\ k_{test}\delta_{ij} \tag{15}$$

$$L_{ij} = -2\widehat{\overline{\rho}} C_\nu \sqrt{k_{test}}\widehat{\Delta}(\langle\tilde{S_{ij}}\rangle - \frac{1}{3}\langle\tilde{S_{ij}}\rangle\delta_{ij}) + \frac{2}{3}\widehat{\overline{\rho}}\ k_{test}\delta_{ij} \tag{16}$$

$$M_{ij} = -\widehat{\overline{\rho}}\ \sqrt{k_{test}}\widehat{\Delta}(\langle\tilde{S_{ij}}\rangle - \frac{1}{3}\langle\tilde{S_{ij}}\rangle\delta_{ij}) \tag{17}$$

A similar approach is used to obtain the dissipation coefficient C_ε such that:

$$C_\epsilon = \frac{\widehat{\Delta}\mu'}{\widehat{\overline{\rho}}\ k_{test}^{3/2}}(\langle\tau_{ij}^{sgs}\frac{\partial u_i}{\partial x_j}\rangle - \langle\overline{\tau}_{ij}^{sgs}\rangle\langle\frac{\partial u_i}{\partial x_j}\rangle) \tag{18}$$

In the above formulation $< f >$ and $\widehat{f}$ both indicate test filtering. More details are given elsewhere.[11,13] There are a few noteworthy points to highlight in the LDKM closure: (a) the LDKM approach does not employ the Germano's identity,[25] (b) the self-similar approach implies that both $\overline{\Delta}$ and $\widehat{\Delta}$ must lie in the inertial range and this provides an estimate for the minimum grid resolution that can be used for a given Re, (c) the denominator in both Eqn. 14 and 18 are well-defined quantities at the test filter level and can be directly computed, (d) the evaluation of the coefficients can be carried out locally (i.e., at all grid points) in space without encountering any instability, (d) the LDKM approach satisfies all the realizability conditions[26] in majority of the grid points even in complex flows, and (e) the dynamic evaluation can be used near walls without any change. Finally, the computational overhead of the LDKM is not very significant since only one additional equation has to be solved.

3 Numerical Method

The LES equations of motion are solved on a three dimensional, boundary-conforming grid using a finite-volume scheme that is fourth-order accurate in space and second-order accurate in time. No-slip, adiabatic wall conditions are used with non-reflecting inflow/outflow boundary conditions.[27]

In general, the computational cost is significant when the compressible solver is employed for

low-speed flow since the explicit time step is restricted by the acoustic speed. However, note that the present study is not focussed on demonstrating an efficient numerical solver, rather it is focussed on demonstrating the ability of LDKM approach (as used in LES) to study high Re wall bounded flow.

In any event, the compressible solver is very efficient on parallel architecture enabling these simulations. The computational domain is distributed in parallel using the Message-Passing Interface (MPI) standard and optimized. The simulation cost is 128.4 CPU nano-sec per time-step per grid-point per processor on the IBM SP4. To reach statistical stationarity, the simulation is carried out for multiple flow through time (τ) over the bump. Typically, $N\tau$ flow through data is averaged (after initial transients are washed out). Simulations were also carried out using a reduced temperature or 30 K instead of 300 K (which decreases the acoustic speed) to increase the explicit time step. Statistical results appear to be insensitive to this change. The mean moments reach stationarity relatively quickly within $Z\tau$, however, the higher moments such as the Reynolds stress take longer to settle down.

Figure 1 shows the geometry for the simulation. The axisymmetric hill height H is 78 mm with the circular base of radius is $2H$. The shape of the hill is defined by:

$$\frac{y(r)}{H} = -\frac{1}{6.04844}[J_o(\Lambda)I_o(\Lambda\frac{r}{a}) - I_o(\Lambda)J_o(\Lambda\frac{r}{a})] \tag{19}$$

where $\Lambda = 3.1926$, J_o is the Bessel function of the first kind, and I_o is modified Bessel function of the first kind. The flow Reynolds number, based on H and inflow velocity (U_{ref}=27.5 m/s), is approximately 1.3×10^5. Figure 1 shows the dimensions of the computational domain in the streamwise and wall-normal directions in terms of the hill-height (H). The zenith of the hill is about $3.4H$ downstream from the inflow boundary and the computational domain extends $6H$ in the spanwise direction and $20H$ in the streamwise direction.

Simulations were conducted initially using different grid but all the results reported here were obtained using the largest grid attemped so far: 256×128×128 grid resolution. For this resolution, the near-wall minimum grid spacing is 56μm in the wall-normal direction. This resolution is chosen so as to give us enough grid points near the surface to reasonably resolve the boundary layer and the separation downstream of the hill. An estimate in terms of the wall units yields minimum (Δx^+, Δy^+, Δz^+) as (12, 4, 100), respectively. Grid clustering is employed in the near-wall and on the lee-side of the hill zenith. However, grid stretching is kept to a minimum, typically less than 2-4 percent in regions of high shear to minimize stretching error. The resolution in the inner boundary layer is considered marginal, and perhaps additional simulations using even higher resolution is warranted. On the other hand, the coarse resolution constraint is consistent with the LES approach pursued here, which is to attempt LES of high Re flows on relatively coarse grids using a higher

order subgrid closure.

Simpson *et al.*[1] report inflow profiles, with nominal speed of U_{ref} and 0.1% freestream turbulence intensity, having boundary layer thickness (δ) of 39 mm and Reynolds number based on momentum thickness (Re_θ) as 7300. Similar mean turbulent boundary layer profile (not shown here) matching above conditions are specified as inflow profile. A Gaussian random field (0.1% of the mean) is added to the inlet velocity profile. This value is as reported.[1] The subgrid kinetic energy intensity in the inlet is also initialized to a 0.1% level. For this low level of inflow turbulence, all the K^{sgs} in the flow is primarily due to production in the boundary layer. Future simulations will revisit inflow by using a more realistic turbulent conditions.

4 Results and Discussion

The $H = 2\delta$ case is analyzed in detail and compared with available data.[1] The smaller bump data is expected to become available soon[28] and therefore, a more detailed comparison for both the cases will be reported later. A word of correction must be mentioned regarding the location where experimental data has been collected. We had been informed by Simpson et al., in a private communication, that the location $x/H = 3.69$ mentioned in their journal paper[1] is incorrect and instead $x/H = 3.63$ must be used for any meaningful comparisons.

The LES time-averaged static pressure coefficient (C_p) is computed here as ($p_{local,static}$ - $p_{ref,static}$) / ($p_{local,total}$ - $p_{ref,static}$). The computed surface distribution of C_p is presented in Fig. 16(a) and the corresponding experimental result[1] is shown in 16(b). For direct comparison, the same number of contour intervals are used in both figures. Four thin-lined concentric circles are shown each representing quarter-radius mark from the center located at the zenith of the axisymmetric hill.

There is remarkable similarity in both features and magnitude between the LES and the experiment. Both results show that as the boundary layer approaches the leading face of the bump, the pressure increases but the increase is not large enough to cause separation. The pressure then decreases at the top of the bump as the flow accelerates (Fig. 3). Maximum (suction) pressure occurs exactly at the top for both cases, but the region is larger in the numerical study. An adverse pressure gradient exists in the lee-side of the bump in both cases, however, adverse pressure region begins later in the computation, perhaps due to the larger low pressure region predicted on the top of the hill. In the spanwise direction both LES and experiments show a nearly symmetric pattern about the center plane parallel to streamwise direction suggesting that the flow is nearly symmetric about that plane. However, symmetry is lost (as will be seen later) on the lee-side, eventhough the surface static pressure contours mentioned above remains nearly symmetric about the center plane, where multiple boundary layer separation occurs.

Flow separation on the lee-side occurs due to the adverse pressure gradient which peaks around the center line parallel to the streamwise direction at the trailing edge of the hill. This region is

at nearly the same location in the computation (Fig. 3(a)) and experiments. There are, however, some differences in the spanwise direction which is more apparent in the flow visualization discussed in the next section.

Figures 3(a) and (b), respectively, represents the static pressure coefficient (C_p) and mean streamwise velocity at the center plane parallel to the streamwise direction. It is important to point out that, while traversing the hill from its foot through the zenith onto its lee-side, at numerous locations the pressure gradient normal to hill surface through the boundary layer is not zero but rather some finite, either negative while approaching or positive around the hill zenith, value. While approaching the hill, sensing streamwise adverse pressure gradient, flow slows down upto around x/H of -2.0 as seen in Fig. 3(b). Then strong streamwise favorable pressure gradient propels the flow up the hill from x/H of -1.0 onwards till it reaches the hill zenith. There on after, faced with stronger streamwise adverse pressure gradient the flow seperates on the lee-side of the hill. Flow-reattachment occurs downstream of the hill thereby forming a turbulent boundary layer which will be measured and compared with.

Figure 3(b) shows no major seperation regions on the lee-side along the center plane from the time-averaged point-of-view. However, we have observed separation regions around x/H of 1.0, albiet small, along the center plane in the instantenous data. One reason contributing to no presence of such regions is owed to our observations of such regions being non-stationary with time and space.

4.1 3D flow separation and reattachment

The flow separation in the lee-side of the bump is quite complex and highly 3D due to both streamwise and spanwise pressure gradients on the lee-side. Figures 4(a) and (b) show respectively, two instantaneous streakline patterns from the LES. These figures show instantaneous pathlines of the fluid and the abrupt termination of a streamline suggests a stagnation point. Multiple stagnation points/regions are seen in these figures. These regions are highly transient and do not show any symmetry in the spanwise direction. Figures 17(a-c) show respectively, the corresponding steady-state streamline pattern, velocity vectors at $y^+ = 8.63$, and the oil flow pattern from the experiment. There are similarities and differences between the instantaneous and steady patterns and also between the LES and the experiment. Multiple regions of recirculation and separation are observed in both studies and many of these features are in good qualitative agreement.

These regions are formed since the fluid motion is in a highly 3D pressure gradient field. The incoming flow accelerates both over the top and around the sides of the hill due to favorable pressure gradient in both direction. However, the magnitude decreases outward from the pressure minimum at the center plane. The flow decelerates in the lee-side with the pressure reaching a maximum at the center plane and just at the end of the bump. The spanwise favorable pressure gradient in the

front causes flow to initially diverge outward, however, in the lee-side this gradient is adverse. This causes the side boundary layers to converge on the back of the bump and closer to the center plane in a high pressure region. In the front and on a portion of the lee-side there is symmetry about the center plane. However, separation occurs in a highly 3D manner, and complex 3D recirculation and re-attachment patterns are seen in the flow. The flow in this region contains both saddle points as well as stagnation points.

The flow field is further analyzed to understand the flow pattern. Figures 6(a-c) shows respectively, the mean streamwise, the mean spanwise, and the mean wall-normal vorticity patterns on the surface of the hill. Bi-level filled-contour pattern (i.e., positive shown as black color and negative shown as white color) is chosen to further exemplify the directional nature of the vorticity patterns over the hill surface. Four thin-lined concentric circles are shown each representing quarter-radius mark. The streamwise vorticity contour, as presented in Fig. 6(a), shows the alternating pattern of the streamwise vorticity while passing the hill.

The streamwise vorticity upstream of the hill zenith has the same orientation as the incoming turbulent boundary layer vorticity. The streamwise vorticity changes direction while passing over the side of the hill and finally it retains its prior direction downstream past the hill. There is intermittent region downstream of the zenith where inter-mingling of the opposite streamwise vortical patterns exists which suggests multiple separation zone of both the sides of the hill zenith. The sign change of the streamwise vorticity while traversing the sides of the hill is owed to the fact of the velocity vector (which for no-slip wall follows the body contour) pointing upwards and then downwards while going up and down the hill making the effective wall-normal velocity component away from and then towards the wall, respectively. The relative strength of the effective wall-normal velocity in spanwise direction determines the orientation of the streamwise vorticity.

Figure 6(b) presents the mean spanwise vorticity over the hill surface. Vortical orientation in the spanwise direction is retained from the incoming turbulent boundary layer by the flow while traversing over the hill surface except over a small region where massive multiple separations are observed. The vortical orientation in that region quickly changes direction (from positive to negative) suggesting flow separation. The region is confined well downstream of the zenith between (in streamwise direction) $x/H = 0.5$ (first circle) and $x/H = 2.0$ (fourth circle) on both sides of the hill. Approximate symmetrical patterns are observed about the center-plane in the spanwise direction. Finally, the mean wall-normal vorticity contours, as presented in Fig. 6(c), shows the multiple separation zones downstream of the hill zenith on both the sides as seen by the counter-rotating wall-normal vortical patterns.

4.1.1 Mean Flow Statistics

Figure 18 shows the spanwise variation of the friction velocity $u_\tau = \sqrt{\tau_w/\rho}$. Here, τ_w is the total shear stress at the wall, taking into account the velocity components in both the streamwise (U) and spanwise (W) direction, at the wall. Specifically, we compute τ_w as equal to $\mu(\frac{\partial Q}{\partial y})_{wall}$, where $Q = \sqrt{U^2 + W^2}$. The predictions are compared with the measurements at the axial location, $x/H = 3.63$. At this location, the flow has re-attached on the wall and the turbulent boundary has reformed. There are some qualitative and quantitative agreement between predictions and measurements. The magnitude of u_τ in both cases agree very well and the general spanwise variation is also qualitatively similar. The computed u_τ shows much more spatial variability than the experimental data. This may be due to two reasons: an inaccuracy in the resolved boundary layer near-wall profile leading to non-physical fluctuations or that since the measurements were at discrete locations, the finer scale variations were not resolved in the experiments. At this point, this issue remains unresolved.

Both results show that the friction velocity increases to a maximum near the center plane $z/H = 0.0$. There are two regions with local maxima observed at around $z/H = -0.5$, and again at around $x/H = -1.2$ in both LES and experiments. The exact locations, however, are slightly different. Both LES and data show that the flow is no longer symmetric about the center plane at this axial location. In general, the peaks in the experimental data are higher than in the LES. The implications of these observations will become apparent in the following discussion.

Figures 19 and 20 show respectively, the normalized (by u_τ) steady-state streamwise and spanwise velocity profiles ($u^+ - y^+, w^+ - y^+$) at $x/H = 3.63$. The LES velocities are normalized using the u_τ values computed earlier. In general, both the computed and measured mean streamwise velocity wall-normal profiles at all the spanwise locations show that a reasonably resolved viscous sublayer exists for $y^+ < 10$ and that a classical log-profile occurs in a region $10 < y^+ < 1000$. The predicted slope is in excellent agreement with measured data. The variability (of the magnitude) in the spanwise direction of the velocity magnitude is similar for both LES and experiments, although in general, the measured profiles are lower in this region. The difference might be due to the higher u_τ in the measurements. We plan to revisit this issue by comparing the unscaled profiles at a later date.

The normalized mean spanwise velocity (w^+) profiles shown in Fig. 20 also show similar qualitative and quantitative agreement with measured data. In general, the magnitude of w^+ is lower in the experiments but this could be due to the aforementioned higher values of measured u_τ. However, the overall wall normal trend is strikingly similar with the velocity changing sign at around $y^+ = 1000$ which is approximately at the end of the log-layer. Beyond $y^+ > 1000$ as the free stream edge is approached, the spanwise motion rapidly decays to zero.

The Reynolds stress (uv^+) profiles are shown in Fig. 21. Both results show similar trend. In general, $uv^+ < 0$ in the boundary layer indicating gradient production of kinetic energy. The LES

predicts a peak at the edge of the log-layer (around $y^+ = 1000$) whereas the experiments suggest a slightly larger peak at a location further away from the wall (around $y^+ = 3000$). In physical dimensions, these locations correspond to about 14 mm and 41 mm respectively. In general, higher order statistics, like Reynolds stress, would take more time to settle in comparison to the first order statistics which is more likely the effect here.

4.2 Time Dependent and Spectral Features

Figures 11(a-c) shows respectively, the iso-surface of the three vorticity components. The vortical structures appear just downstream of the zenith of the hill where multiple separation zones are observed. Initially, the structures have some coherence (as seen by smooth and continuous iso-surface for a relatively longer spatial distance) upstream of the hill but subsequently, these structures breakdown into small-scale randomly oriented structures. The vorticity field appears to be highly 3D with no component dominating in the 3D separation/re-attachment regions.

Figure 12 shows normal stresses $(\overline{u^2}, \overline{v^2}, \overline{w^2})$ at $x/H = 3.63$ and $y^+ = 787$ plotted spanwise about the hill center line. We observe that each individual normal stress peaks on either side of the center line around z/H of 0.5. An-isotropic behaviour is observed by noticing higher peaks for the streamwise normal stress as related to the wall-normal and spanwise normal stresses.

Figure 20 shows that the mean spanwise velocity switches direction on either side of the center line. This indicates the presence of strong streamwise counter-rotating vortex pair centered around $z/H = 0.0$. Figure 13(a) shows the secondary flow vector field at the measurement plane. We observe the presence of streamwise counter-rotating vortex pair located about y/H of 0.25 above the surface and centered around $z/H = 0.0$. We also observe large turbulence levels away from the wall around the hill center line as seen in Fig. 13(b) where $TKE = \overline{q^2}/2 = (\overline{u^2} + \overline{v^2} + \overline{w^2})/2$. The higher turbulence levels are contributed to the presence of strong streamwise vortices as indicated by the secondary flow streamlines. This is consistent with the observations of Simpson *et al.*[1]

Spectral analysis of the velocity fluctuations is also carried to investigate the spectral content of the flow. Figure 14 shows the streamwise and spanwise velocity component spectra. The inertial range $-5/3$ slope is also shown. There is a small representation of the inertial region in the edge of the log layer ($y^+ = 787$).

Figure 15 shows the characteristic pressure spectra at the same location. There is no specific peak in the spectra indicating a broadband acoustic emission at this location. Future study will investigate the instantaneous features and the near field acoustics in more detail.

5 Conclusions

Large-Eddy Simulation (LES) with a Localized Dynamic subgrid Kinetic energy Model (LDKM) is used to simulate high Re turbulent flow over an axisymmetric hill of height $H = 2\delta$. Surface pressure distribution, flow patterns and mean flow properties are compared with experimental

observations. Most of the measured features are reproduced qualitatively and in some cases, quantitatively by the LES. The surface pressure distribution and the formation of the multiple recirculation regions seen in the experiments is well reproduced in the simulation. Some differences in the lee-side where complex 3D separation and re-attachment occurs are also observed and discussed. These results suggest that the LDKM approach has the ability to capture complex near-wall high-Re features using a resolution that is reasonable for LES studies. It is believed that this ability is achieved in LDKM due to two features: the characteristic velocity scale for the subgrid fluctuation is explicitly computed in LDKM, and hence, its effect on the resolved motion is properly included, and, the localized dynamic approach used in the LDKM approach provides a robust method to compute the model coefficients everywhere without requiring any averaging or smoothing.

Future studies will revisit this bump case using a new subgrid simulation model[9,10] as well as using LDKM but with improved inflow turbulence. Finally, simulations of the flow past the $H = \delta$ case will be completed (these simulations are currently underway) and analyzed.

6 Acknowledgments

This work is supported by the Office of Naval Research (ONR). High Performance Computing (HPC) resources are provided by the Department of Defense (DOD) Major Shared Resources Centers (MSRC) at Naval Oceanographic Office (NAVOCEANO), and Maui High Performance Computing Center (MHPCC).

References

[1] Simpson, R., Long, C., and Byun, G., "Study of vortical separation from an axisymmetric hill," *International Journal of Heat and Fluid Flow*, Vol. 23, 2002, pp. 582–591.

[2] Simpson, R., "Structure of Rough-wall Three-dimensional Turbulent Boundary Layers and Vortical Separations," *2001 Turbulence and Wakes Program Review, Office of Naval Research*, 2001.

[3] Piomelli, U., "High Reynolds Number Calculations Using the Dynamic Subgrid-Scale Stress Model," *Physics of Fluids A*, Vol. 5, No. 6, 1993, pp. 1484–1484.

[4] Piomelli, U. and Liu, J., "Large-Eddy Simulation of Rotating Channel Flows Using a Localized Dynamic Model," *Physics of Fluids*, Vol. 7, No. 4, 1995, pp. 839–839.

[5] Fureby, C., "Large eddy simulations of anisochoric flows," *AIAA J.*, Vol. 33, 1994, pp. 1263–1272.

[6] Balaras, E., Benocci, C., and Piomelli, U., "Two-layer approximate boundary conditions for large-eddy simulations," *AIAA J.*, Vol. 34, 1996, pp. 1111–1119.

[7] Cabot, W., "Large-eddy simulations with wall models," *Center For Turbulent Research, Annual Research Briefs*, 1995, pp. 41–49.

[8] Spalart, P. R., "Strategies for turbulence modelling and simulations," *International Journal of Heat and Fluid Flow*, Vol. 21, 2000, pp. 252–263.

[9] Kemenov, K. and Menon, S., "TLS: A new two level simulation methodology for high Re LES," *AIAA 2002-0287*, 2002.

[10] Menon, S. and Kemenov, K., "A Two-Level Simulation Methodology for LES of High Reynolds Number Flows," *Advances in Turbulence IX*, 2002, pp. 329–352.

[11] Menon, S. and Kim, W.-W., "High Reynolds number flow simulations using the localized dynamic subgrid-scale model," *AIAA Paper 96–0425*, 1996.

[12] Kim, W.-W. and Menon, S., "Application of the localized dynamic subgrid-scale model to turbulent wall-bounded flows," *AIAA Paper 97–0210*, 1997.

[13] Kim, W.-W., Menon, S., and Mongia, H. C., "A new incompressible solver for Large-Eddy Simulations," *International Journal of Numerical Fluid Mechanics*, Vol. 31, 1999, pp. 983–1017.

[14] Kim, W.-W., Menon, S., and Mongia, H. C., "Large eddy simulations of a gas turbine combustor flow," *Combustion Science and Technology*, Vol. 143, 1999, pp. 25–62.

[15] Kim, W.-W. and Menon, S., "Numerical Simulations of Turbulent Premixed Flames in the Thin-Reaction-Zones Regime," *Combustion Science and Technology*, Vol. 160, 2000, pp. 119–150.

[16] Chakravathy, V. K. and Menon, S., "Subgrid Modeling of Turbulent Premixed Flames in the Flamelet Regime," *Flow, Turbulence and Combustion*, Vol. 5, 2000, pp. 23–45.

[17] Menon, S., "Subgrid combustion modelling for LES of single and two-phase reacting flows," *Advances in LES of Complex Flows*, 2000, pp. 329–352.

[18] Nelson, C. C. and Menon, S., "Unsteady Simulations of Compressible Spatial Mixing Layers," *AIAA-98-0786*, 1998.

[19] Jou, W.-H. and Menon, S., "Modes of Oscillation in a Nonreacting Ramjet combustor Flow," *Journal of Propulsion and Power*, Vol. 6, No. 5, 1990, pp. 535–543.

[20] Erlebacher, G., Hussaini, M. Y., Speziale, C. G., and Zang, T. A., "Toward the Large-Eddy Simulation of Compressible Turbulent Flows," *Journal of Fluid Mechanics*, Vol. 238, 1992, pp. 155–185.

[21] Smagorinsky, J., "General Circulation Experiments with the Primitive Equations," *Monthly Weather Review*, Vol. 91, No. 3, 1993, pp. 99–164.

[22] Schumann, U., "Subgrid scale model for finite difference simulations of turbulent flows in plane channels and annuli." *Journal of Computational Physics*, Vol. 18, 1975, pp. 376–404.

[23] Menon, S., Yeung, P.-K., and Kim, W.-W., "Effect of Subgrid Models on the Computed Interscale Energy Transfer in Isotropic Turbulence," *Computers and Fluids*, Vol. 25, No. 2, 1996, pp. 165–180.

[24] Liu, S., Meneveau, C., and Katz, J., "On the Properties of Similarity Subgrid-Scale Models as Deduced from Measurements in a Turbulent Jet," *Journal of Fluid Mechanics*, Vol. 275, 1994, pp. 83–119.

[25] Germano, M., Piomelli, U., Moin, P., and Cabot, W. H., "A Dynamic Subgrid-Scale Eddy viscosity Model," *Physics of Fluids A*, Vol. 3, No. 11, 1991, pp. 1760–1765.

[26] Schumann, U., "Realizability of Reynolds-Stress Turbulence Models," *Physics of Fluids*, Vol. 20, No. 5, 1977, pp. 721–725.

[27] Poinsot, T. and Lele, S., "Boundary conditions for direct simulations of compressible viscous flow," *Journal of Computational Physics*, Vol. 101, 1992, pp. 104–129.

[28] Byun, G., Simpson, R., and Long, C., "Study of vortical separation from Three-Dimensional symmetric bumps," *AIAA Paper 03–0641 (To appear)*, 2003.

List of Figure Captions

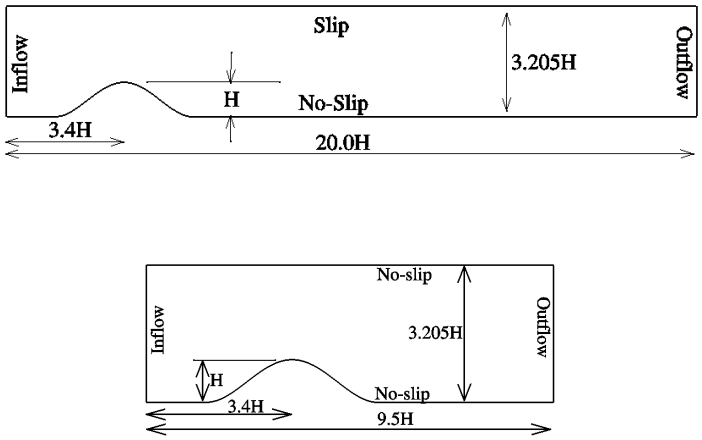
Slip
Inflow
Outflow
3.205H
H
No-Slip
3.4H
20.0H
No-slip
Inflow
3.205H
Outflow
H
No-slip
3.4H
9.5H

FIGURE 1

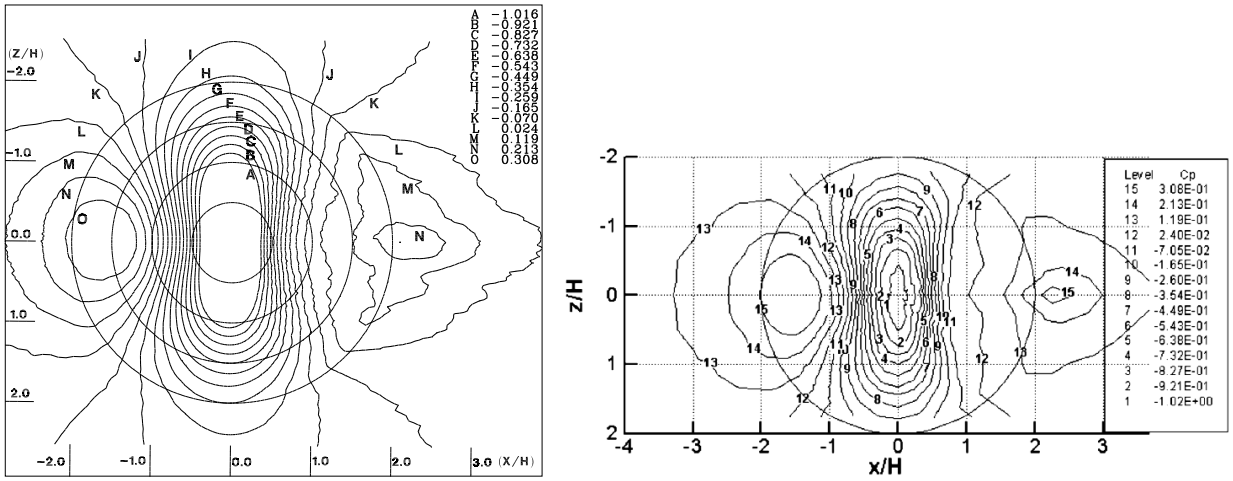
(Z/H)
-2.0
-1.0
0.0
1.0
2.0
-2.0
-1.0
0.0
1.0
2.0
3.0 (X/H)
A -1.016
B -0.921
C -0.827
D -0.732
E -0.638
F -0.543
G -0.449
H -0.354
I -0.259
J -0.165
K -0.070
L 0.024
M 0.119
N 0.213
O 0.308
z/H
x/H
-4
-3
-2
-1
0
1
2
3
-2
-1
0
1
2
Level Cp
15 3.08E-01
14 2.13E-01
13 1.19E-01
12 2.40E-02
11 -7.05E-02
10 -1.65E-01
9 -2.60E-01
8 -3.54E-01
7 -4.49E-01
6 -5.43E-01
5 -6.38E-01
4 -7.32E-01
3 -8.27E-01
2 -9.21E-01
1 -1.02E+00

Figure 2

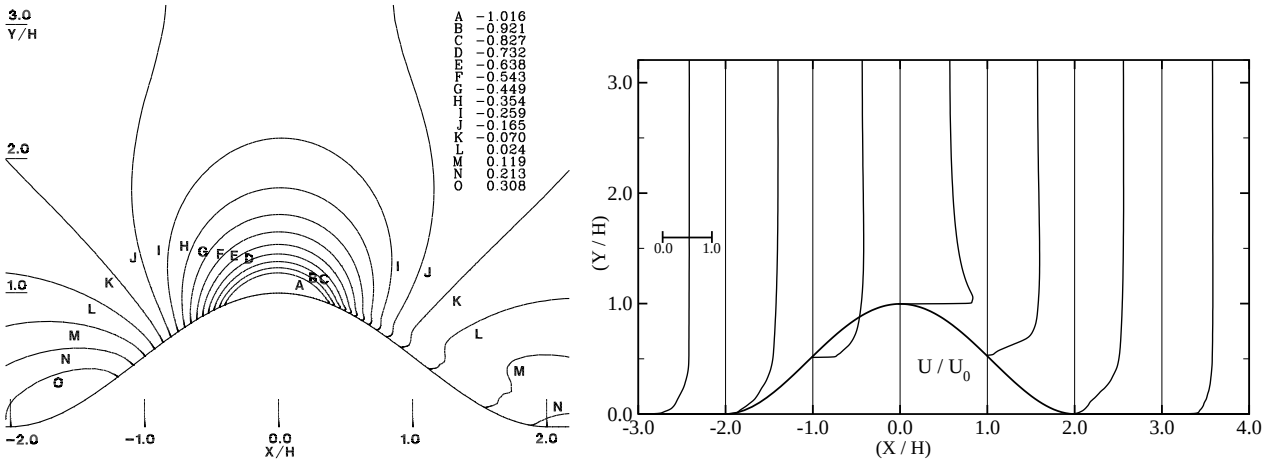
3.0
Y/H
2.0
1.0
−2.0
−1.0
0.0
X/H
1.0
2.0
A −1.016
B −0.921
C −0.827
D −0.732
E −0.638
F −0.543
G −0.449
H −0.354
I −0.259
J −0.165
K −0.070
L 0.024
M 0.119
N 0.213
O 0.308
0.0
1.0
U / U0
(Y / H)
(X / H)
-3.0
-2.0
-1.0
0.0
1.0
2.0
3.0
4.0

FIGURE 3

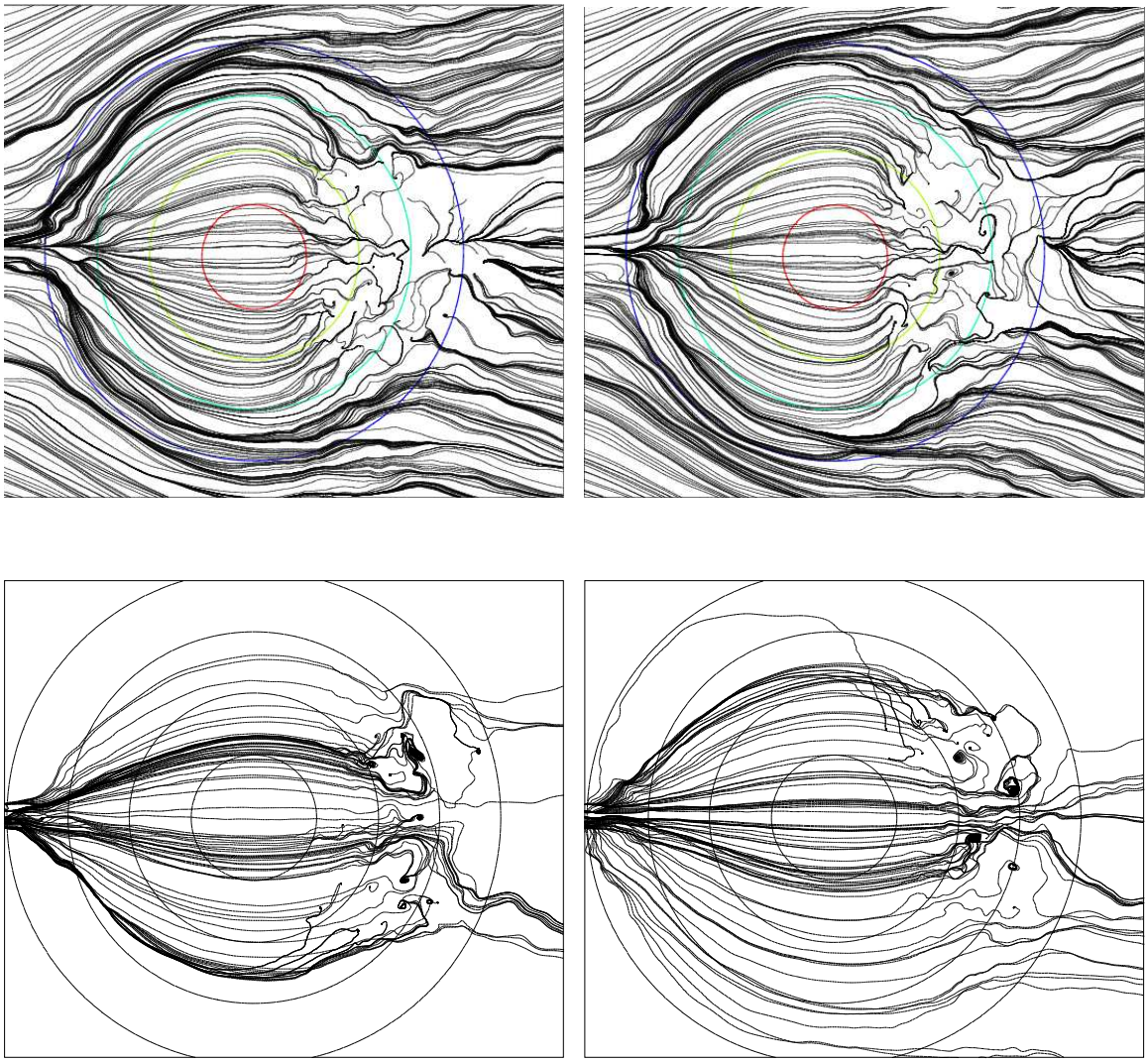

FIGURE 4

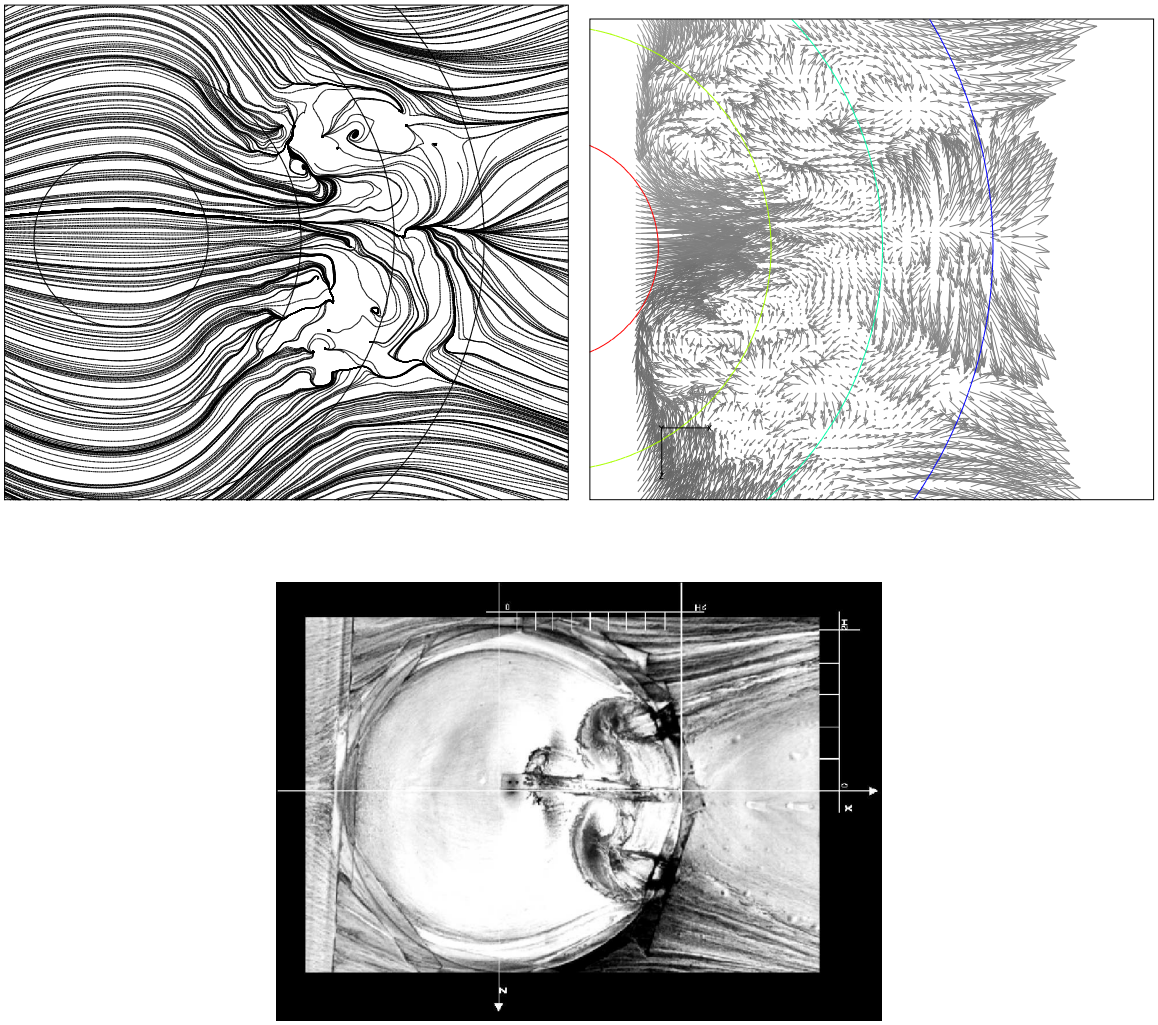

Figure 5

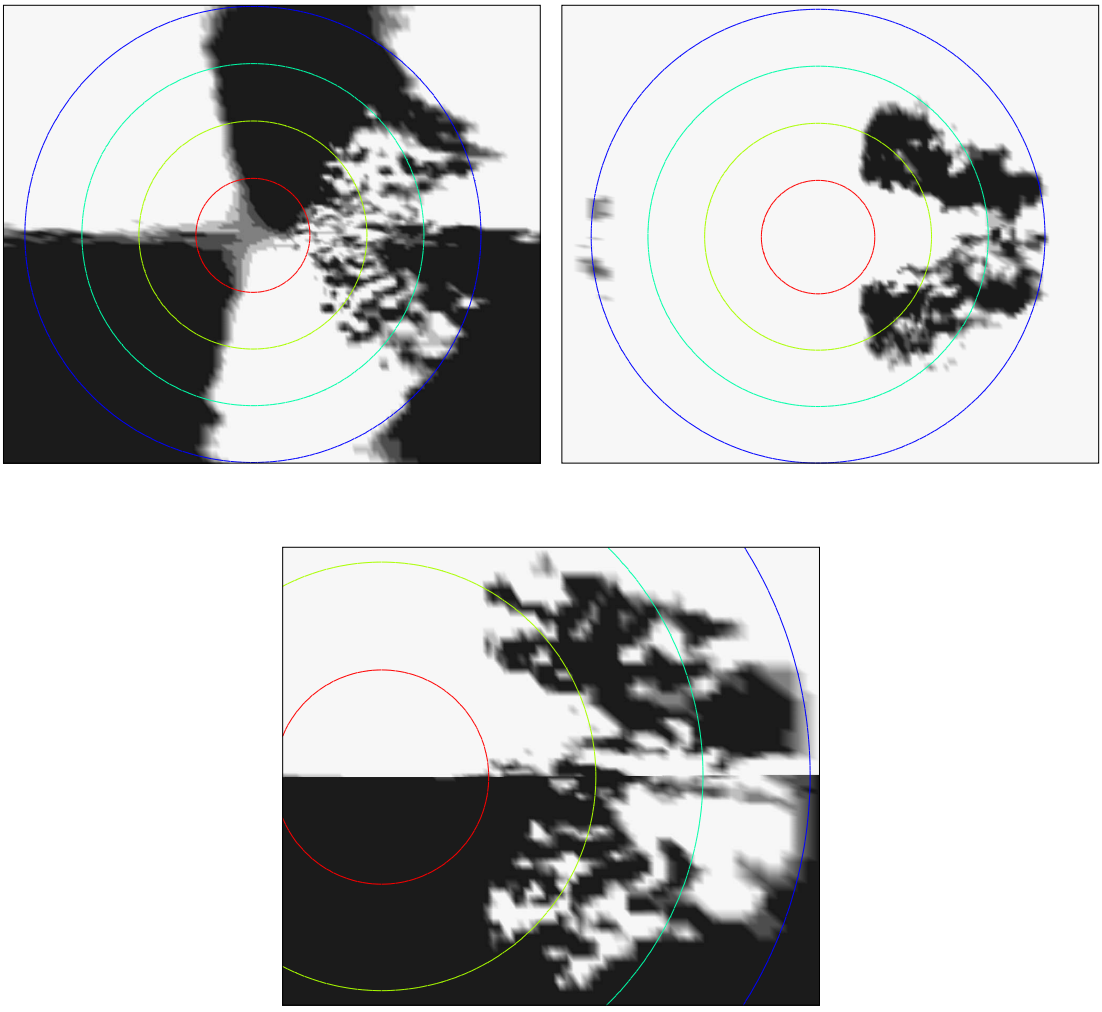

FIGURE 6

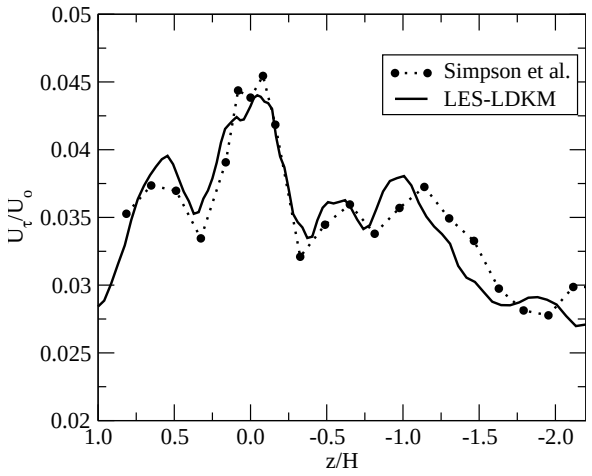
0.05
0.045
0.04
0.035
0.03
0.025
0.02
1.0
0.5
0.0
-0.5
-1.0
-1.5
-2.0
z/H
U_t/U_o
Simpson et al.
LES-LDKM

FIGURE 7

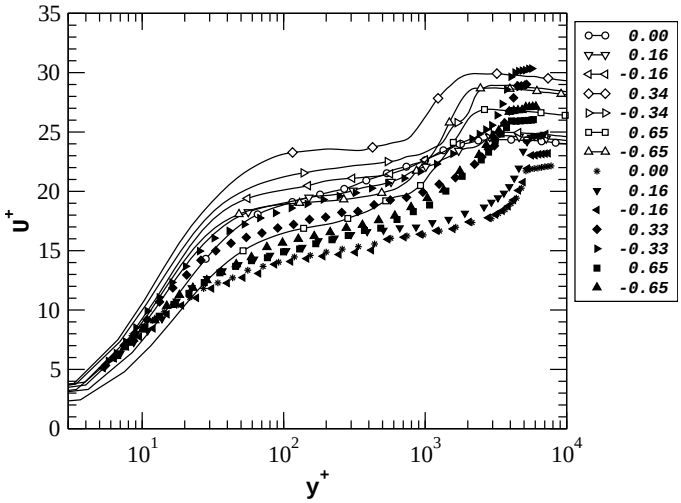
35
30
25
20
15
10
5
0
U+
10^1
10^2
10^3
10^4
y+
0.00
0.16
-0.16
0.34
-0.34
0.65
-0.65
0.00
0.16
-0.16
0.33
-0.33
0.65
-0.65

FIGURE 8

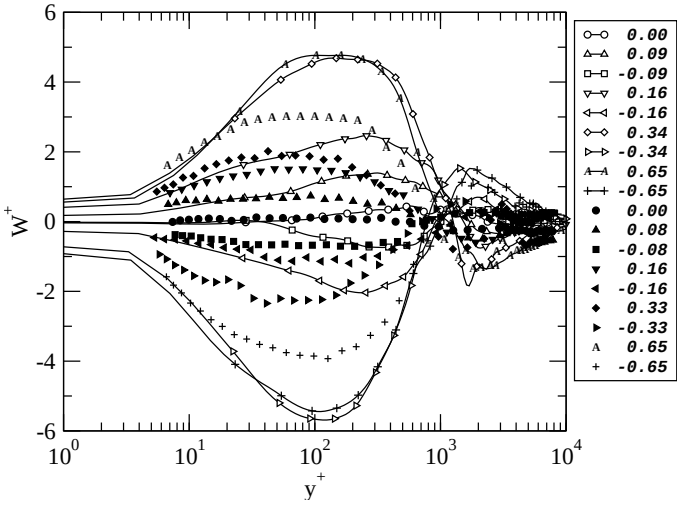
6
4
2
0
-2
-4
-6
10^0
10^1
10^2
10^3
10^4
W^+
y^+
0.00
0.09
-0.09
0.16
-0.16
0.34
-0.34
0.65
-0.65
0.00
0.08
-0.08
0.16
-0.16
0.33
-0.33
0.65
-0.65

FIGURE 9

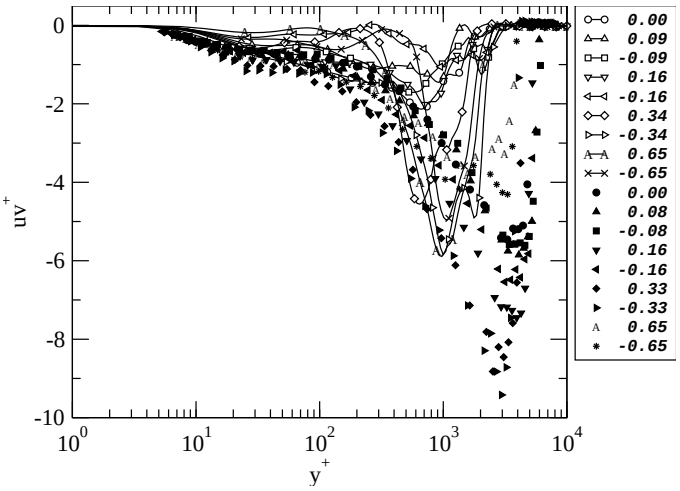
0.00
0.09
-0.09
0.16
-0.16
0.34
-0.34
0.65
-0.65
0.00
0.08
-0.08
0.16
-0.16
0.33
-0.33
0.65
-0.65
uv+
y+

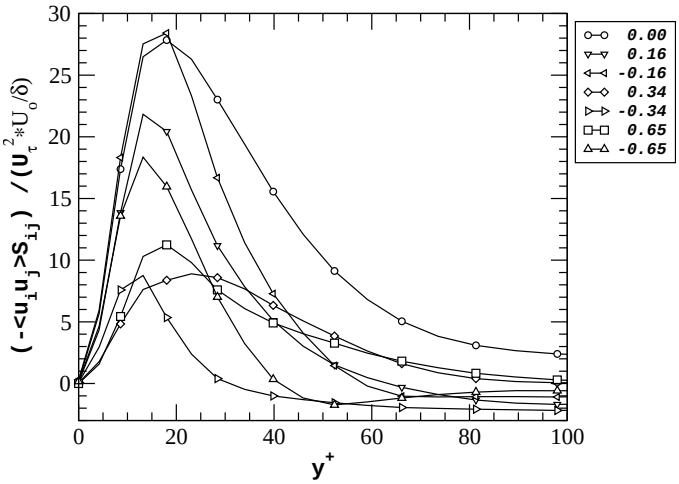
0.00
0.16
-0.16
0.34
-0.34
0.65
-0.65
(-<uiuj>Sij) /(uτ2*Uo/δ)
y+

FIGURE 10

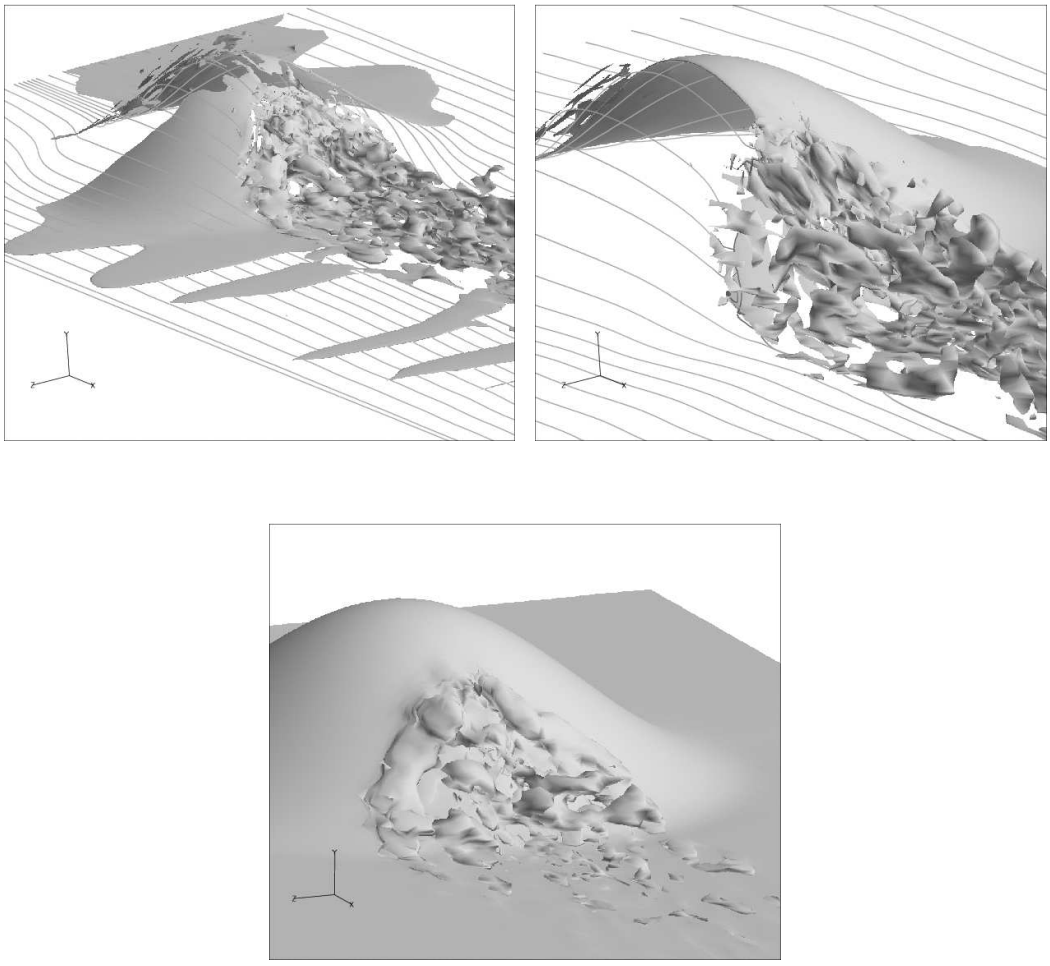

Figure 11

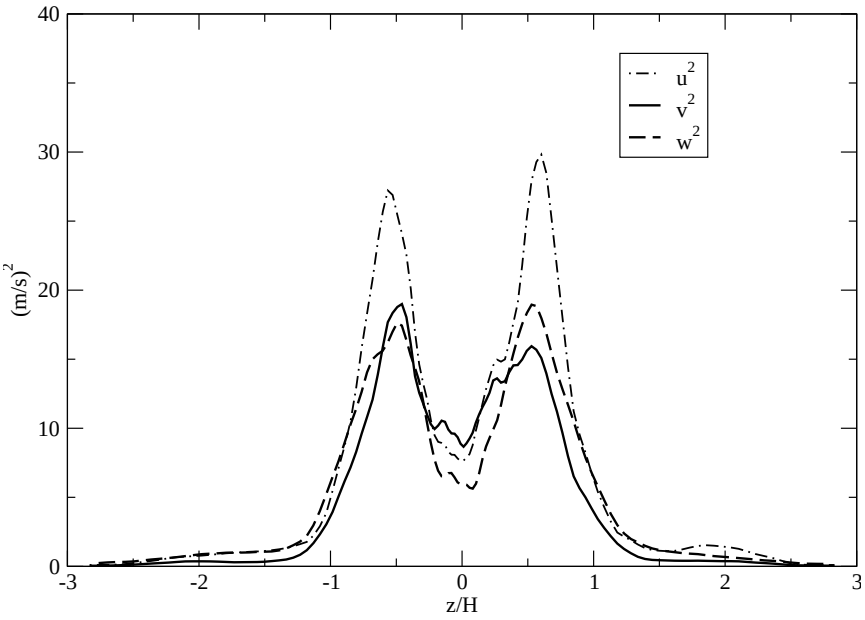

FIGURE 12

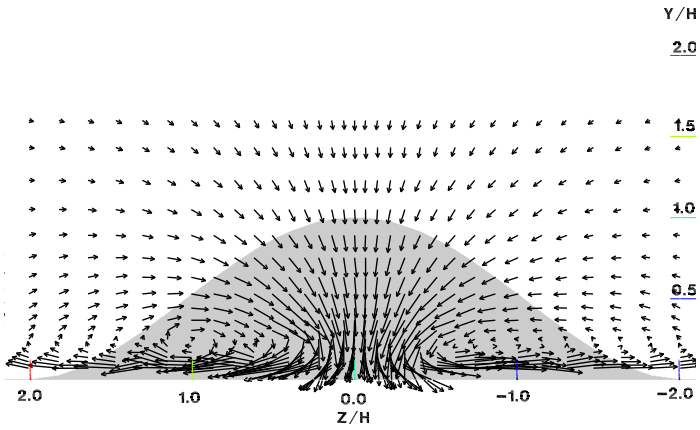
Y/H
2.0
1.5
1.0
0.5
2.0
1.0
0.0
−1.0
−2.0
Z/H

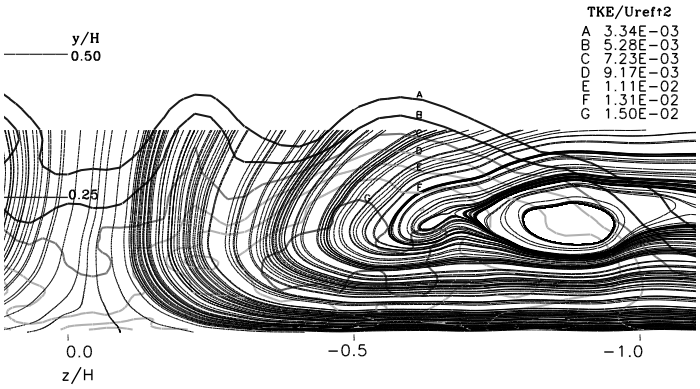
y/H
0.50
0.25
TKE/Uref2
A 3.34E−03
B 5.28E−03
C 7.23E−03
D 9.17E−03
E 1.11E−02
F 1.31E−02
G 1.50E−02
0.0
−0.5
−1.0
z/H

Figure 13

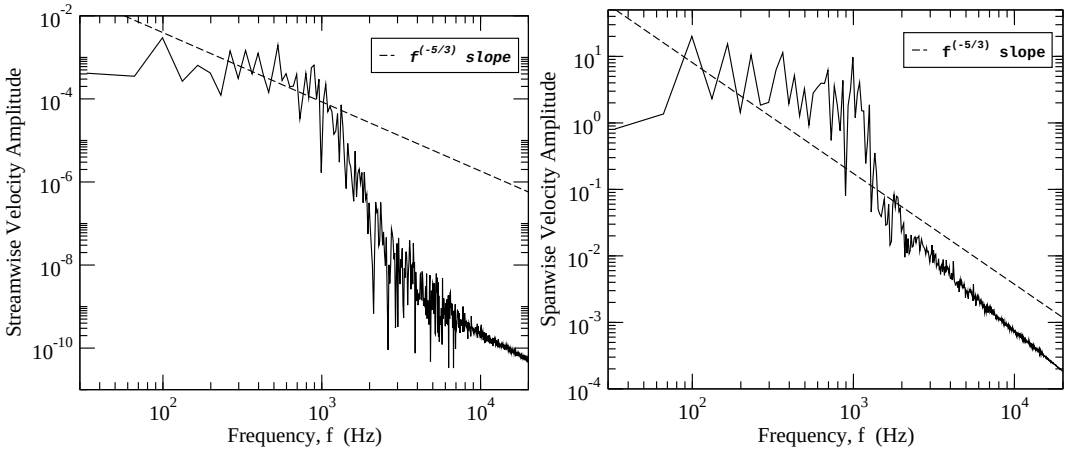
Streamwise Velocity Amplitude
Frequency, f (Hz)
f^(-5/3) slope
Spanwise Velocity Amplitude
Frequency, f (Hz)
f^(-5/3) slope

FIGURE 14

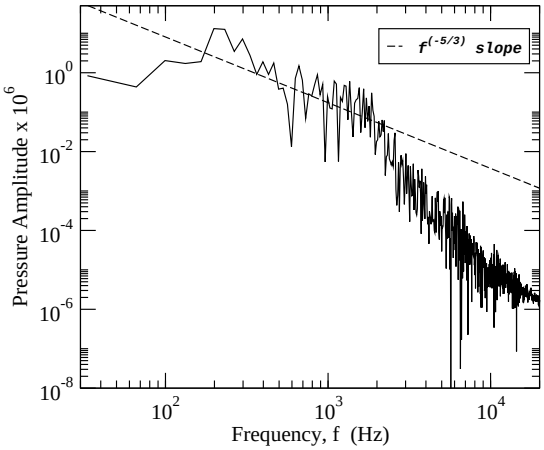
f^(-5/3) slope
Pressure Amplitude x 10^6
10^0
10^-2
10^-4
10^-6
10^-8
10^2
10^3
10^4
Frequency, f (Hz)

FIGURE 15

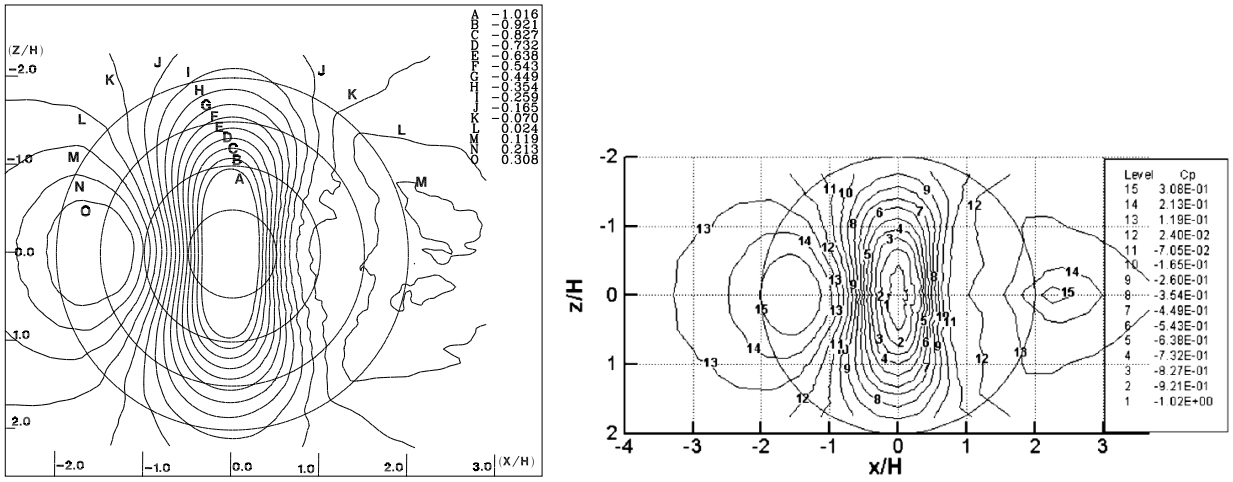
(Z/H)
-2.0
-1.0
0.0
1.0
2.0
(X/H)
A -1.016
B -0.921
C -0.827
D -0.732
E -0.638
F -0.543
G -0.449
H -0.354
I -0.259
J -0.165
K -0.070
L 0.024
M 0.119
N 0.213
O 0.308
z/H
x/H
Level Cp
15 3.08E-01
14 2.13E-01
13 1.19E-01
12 2.40E-02
11 -7.05E-02
10 -1.65E-01
9 -2.60E-01
8 -3.54E-01
7 -4.49E-01
6 -5.43E-01
5 -6.38E-01
4 -7.32E-01
3 -8.27E-01
2 -9.21E-01
1 -1.02E+00

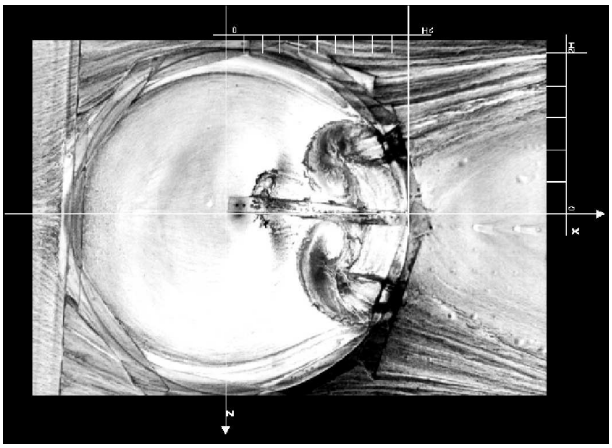

Figure 17

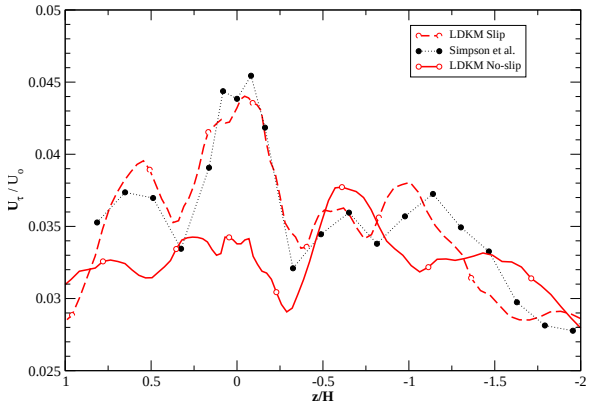
LDKM Slip
Simpson et al.
LDKM No-slip
0.05
0.045
0.04
0.035
0.03
0.025
U_t / U_o
1
0.5
0
-0.5
-1
-1.5
-2
z/H

Figure 18

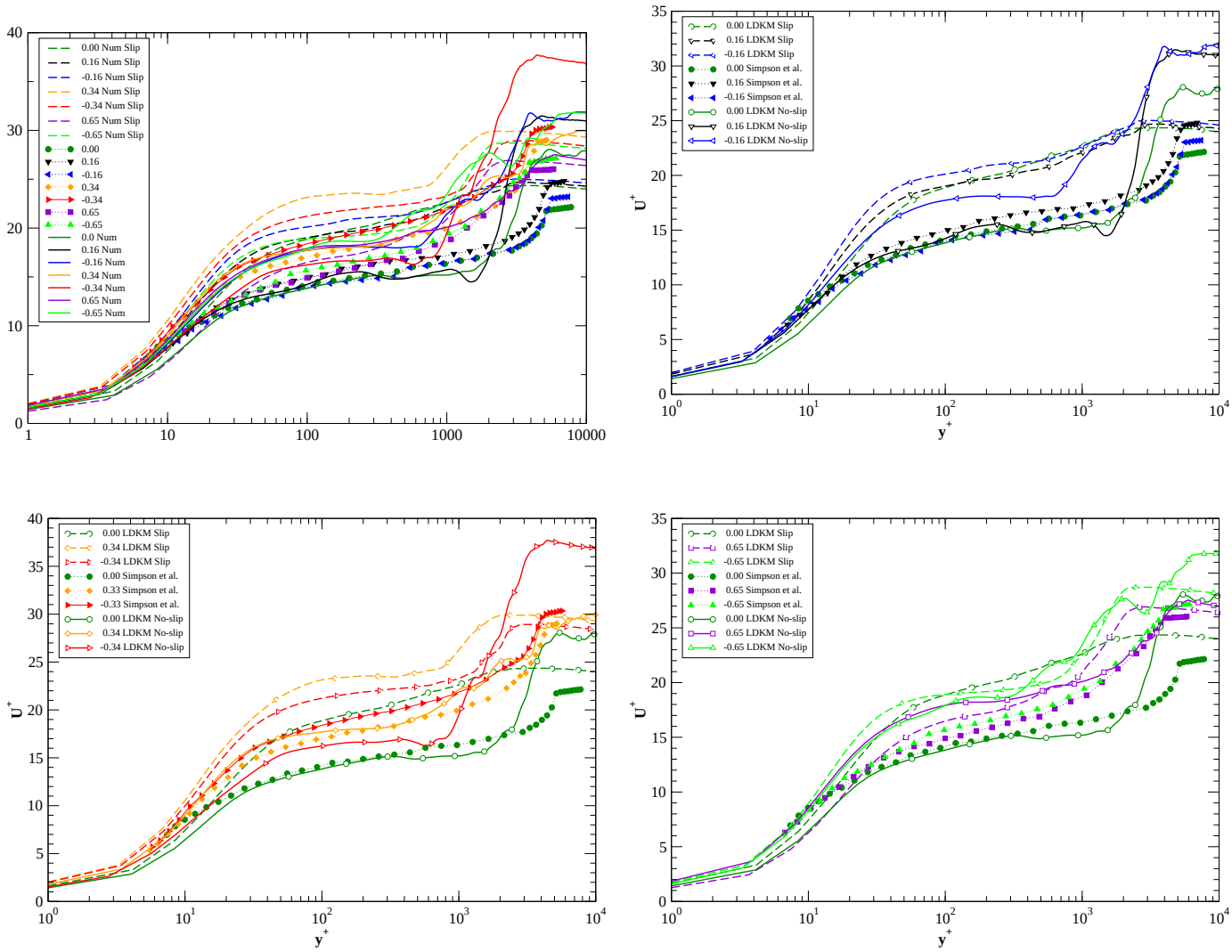
0.00 Num Slip
0.16 Num Slip
-0.16 Num Slip
0.34 Num Slip
-0.34 Num Slip
0.65 Num Slip
-0.65 Num Slip
0.00
0.16
-0.16
0.34
-0.34
0.65
-0.65
0.0 Num
0.16 Num
-0.16 Num
0.34 Num
-0.34 Num
0.65 Num
-0.65 Num
0.00 LDKM Slip
0.16 LDKM Slip
-0.16 LDKM Slip
0.00 Simpson et al.
0.16 Simpson et al.
-0.16 Simpson et al.
0.00 LDKM No-slip
0.16 LDKM No-slip
-0.16 LDKM No-slip
0.00 LDKM Slip
0.34 LDKM Slip
-0.34 LDKM Slip
0.00 Simpson et al.
0.33 Simpson et al.
-0.33 Simpson et al.
0.00 LDKM No-slip
0.34 LDKM No-slip
-0.34 LDKM No-slip
0.00 LDKM Slip
0.65 LDKM Slip
-0.65 LDKM Slip
0.00 Simpson et al.
0.65 Simpson et al.
-0.65 Simpson et al.
0.00 LDKM No-slip
0.65 LDKM No-slip
-0.65 LDKM No-slip
U+
y+

FIGURE 19

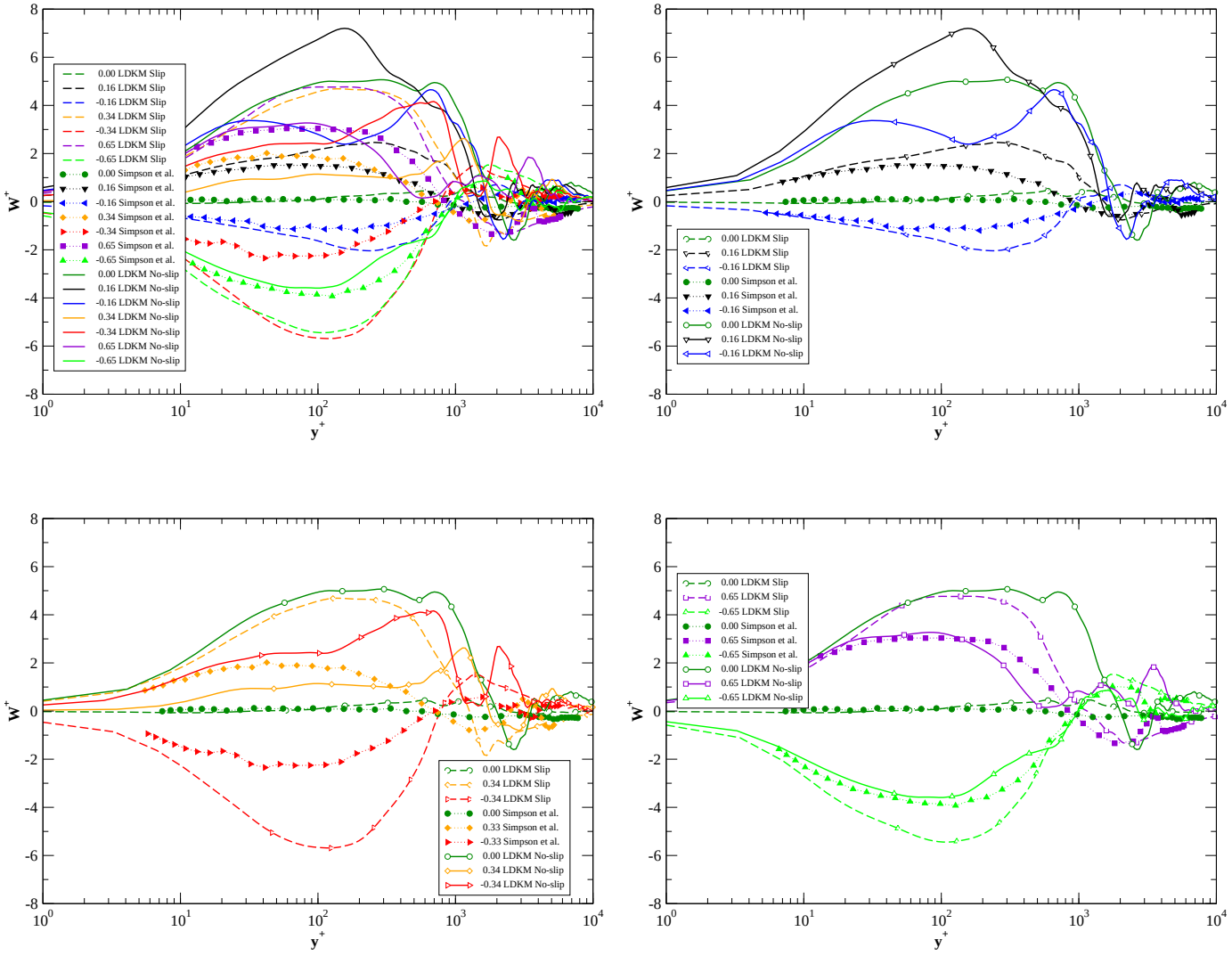
w+
y+
0.00 LDKM Slip
0.16 LDKM Slip
-0.16 LDKM Slip
0.34 LDKM Slip
-0.34 LDKM Slip
0.65 LDKM Slip
-0.65 LDKM Slip
0.00 Simpson et al.
0.16 Simpson et al.
-0.16 Simpson et al.
0.34 Simpson et al.
-0.34 Simpson et al.
0.65 Simpson et al.
-0.65 Simpson et al.
0.00 LDKM No-slip
0.16 LDKM No-slip
-0.16 LDKM No-slip
0.34 LDKM No-slip
-0.34 LDKM No-slip
0.65 LDKM No-slip
-0.65 LDKM No-slip
0.33 Simpson et al.
-0.33 Simpson et al.

FIGURE 20

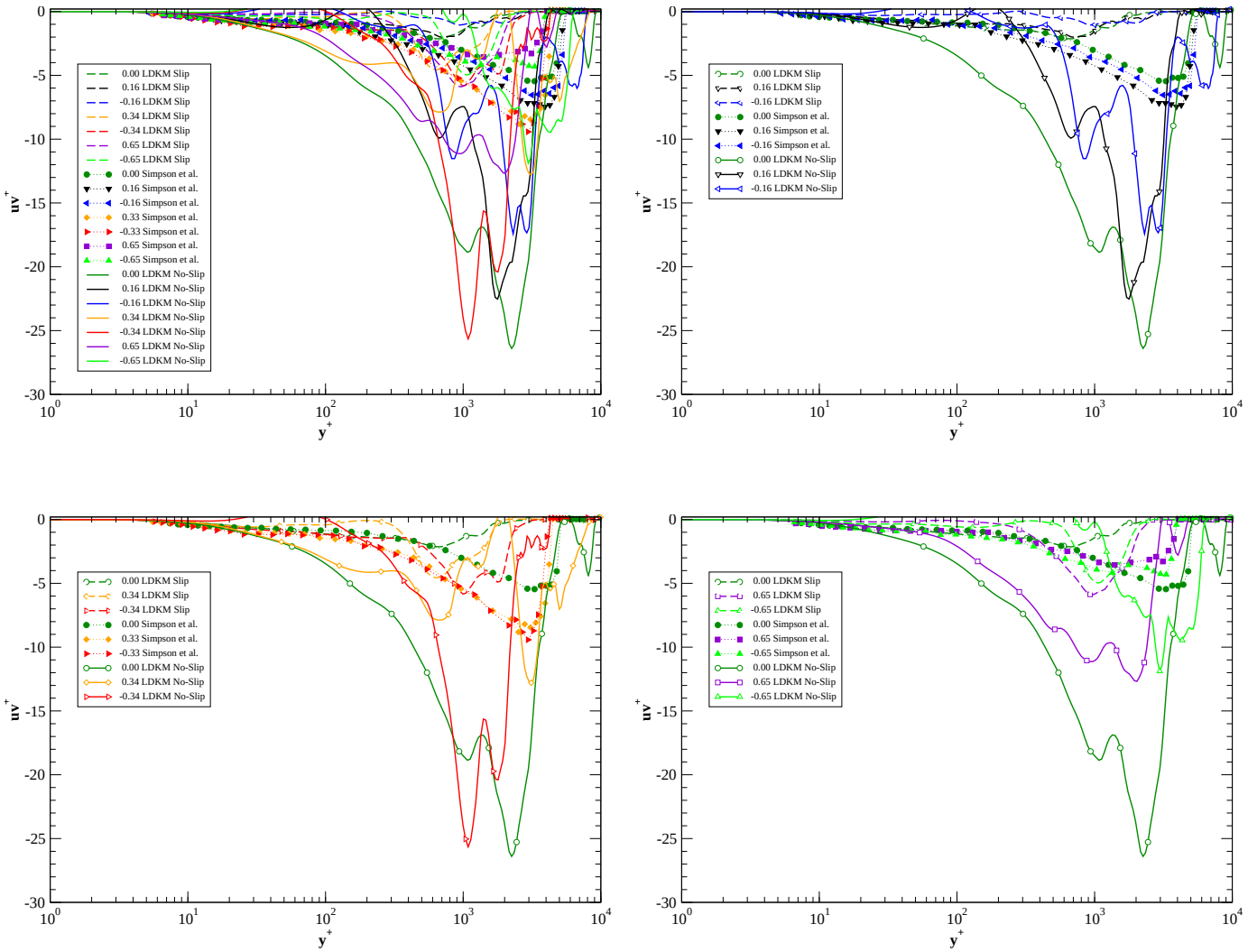
0.00 LDKM Slip
0.16 LDKM Slip
-0.16 LDKM Slip
0.34 LDKM Slip
-0.34 LDKM Slip
0.65 LDKM Slip
-0.65 LDKM Slip
0.00 Simpson et al.
0.16 Simpson et al.
-0.16 Simpson et al.
0.33 Simpson et al.
-0.33 Simpson et al.
0.65 Simpson et al.
-0.65 Simpson et al.
0.00 LDKM No-Slip
0.16 LDKM No-Slip
-0.16 LDKM No-Slip
0.34 LDKM No-Slip
-0.34 LDKM No-Slip
0.65 LDKM No-Slip
-0.65 LDKM No-Slip
uv+
y+

Figure 21